

Transit Lightcurves of Extrasolar Planets Orbiting Rapidly-Rotating Stars

Jason W. Barnes

Department of Physics

University of Idaho

Moscow, ID 83844-0903

ResearcherID: B-1284-2009

jwbarnes@uidaho.edu

ABSTRACT

Main-sequence stars earlier than spectral type \sim F6 or so are expected to rotate rapidly due to their radiative exteriors. This rapid rotation leads to an oblate stellar figure. It also induces the photosphere to be hotter (by up to several thousand Kelvin) at the pole than at the equator as a result of a process called gravity darkening that was first predicted by von Zeipel (1924). Transits of extrasolar planets across such a non-uniform, oblate disk yield unusual and distinctive lightcurves that can be used to determine the relative alignment of the stellar rotation pole and the planet orbit normal. This spin-orbit alignment can be used to constrain models of planet formation and evolution. Orderly planet formation and migration within a disk that is coplanar with the stellar equator will result in spin-orbit alignment. More violent planet-planet scattering events should yield spin-orbit misaligned planets. Rossiter-McLaughlin measurements of transits of lower-mass stars show that some planets are spin-orbit aligned, and some are not. Since Rossiter-McLaughlin measurements are difficult around rapid rotators, lightcurve photometry may be the best way to determine the spin-orbit alignment of planets around massive stars. The *Kepler* mission will monitor $\sim 10^4$ of these stars within its sample. The lightcurves of any detected planets will allow us to probe the planet formation process around high-mass stars for the first time.

Subject headings: techniques:photometric — eclipses — Stars:individual:Altair

1. INTRODUCTION

Fifty-five transiting extrasolar planets have been discovered to date (see <http://exoplanet.eu/>). Most of these planets orbit stars that have masses near $1 M_{\odot}$. The primary reasons for this parent star mass bias for transiting planets are twofold: (1) stars of spectral type later than K are too dim to be caught in large numbers by wide-field transit surveys, and (2) stars earlier than F have rotationally broadened spectral lines and inherent stellar noise that make high-precision radial velocity follow-up impossible at present.

To address the early-star radial velocity problem, Johnson et al. (2007) used radial velocity to survey evolved high-mass stars that were formerly early-type dwarfs when they were on the main sequence. Johnson et al. (2007) and Johnson et al. (2008a) described 11 known planets around evolved stars with $1.5 M_{\odot} < M_{*} < 3.0 M_{\odot}$, presumably former A stars. Since then 14 new planets around high-mass stars have been found: NGC4349#127b (Lovis & Mayor 2007), 81 Cetus b (Sato et al. 2008b), NGC2423#3b (Lovis & Mayor 2007), 18 Delphinus b (Sato et al. 2008a), HD17092b (Niedzielski et al. 2007), 14 Andromedae b (Sato et al. 2008b), ξ Aquilae b (Sato et al. 2008a), HD81688b (Sato et al. 2008a), HD173416b (Liu et al. 2009), HD102272b and HD102272c (Niedzielski et al. 2008), 6 Lyncis b (Sato et al. 2008b), HD5319b (Robinson et al. 2007), and OGLE2-TR-L9b (Snellen et al. 2008). The

last of these, OGLE-2-TR-L9b, is the only radial velocity planet whose host star has $M_{*} > 1.5 M_{\odot}$ and lies on the main sequence (spectral type F3V), and this planet is the only one that is known to transit a massive star as well.

The *Kepler* mission will discover many more transiting planets around early-type stars, if they exist. At least 10,000 main-sequence stars earlier than spectral type F5 should be present in the *Kepler* field, and will presumably be among the mission's targets. *Kepler* will then be able to characterize the distribution of planets with short periods around high-mass stars. These close-in planets will complement the far-out planets recently discovered around A dwarfs using direct imaging (Marois et al. 2008; Kalas et al. 2008), and lead to a better understanding of how planet formation varies with stellar mass.

Main sequence stars earlier than \sim mid-F spectral type, those with $M \gtrsim 1.5 M_{\odot}$, are all expected to be fast rotators. The structure of these stars is such that they have radiative zones in their outermost layers, instead of a convective zone near the surface like for our Sun. The exterior convection in later-type stars drives surface magnetic activity, which in turn drives strong stellar winds that sap the star's angular momentum with time. Early-type, exterior-radiative stars retain their youthful high angular momenta, with some spinning at near the breakup speed (e.g. Hansen et al. 2004, and references therein). As a result, early-type main sequence stars can be significantly oblate.

The rotation induces an equator-to-pole gradient in the effective acceleration due to gravity g at the surface. von Zeipel (1924) showed that in such a case the temperature of the star varies from equator to pole as well, a phenomenon called gravity-darkening. The Von Zeipel Theorem thus predicts that the flux emitted from the surface of a rapidly rotating star is proportional to the local effective gravity. Thus the effect induces cooler temperatures (and hence lower emitted fluxes) at a star’s equator, and hotter temperatures at the poles. The basic predictions of von Zeipel theory were dramatically confirmed by recent optical interferometric observations of Vega (α Lyrae) (Peterson et al. 2006b, explaining residuals in earlier near-IR interferometry by Ciardi et al. (2001).) and Altair (α Aquilae) (Monnier et al. 2007). Gravity darkening is used regularly to characterize close binary star systems from their lightcurves (*i.e.* Djurašević et al. 2003). In binary systems that interact gravitationally, tides can also reduce the effective gravity, resulting in gravity darkening.

If planets around fast-rotating stars formed in-situ from the protostellar disk or migrated to their present locations within that disk, then those planets might be expected to orbit near their stars’ equatorial planes. If those planets transit, then their orbital inclinations i are near 90° (using radial velocity teams’ definition of i as the angle between the planet’s orbit pole and the plane of the sky). The stellar orbit pole would then be nearly coincident with the planet’s orbit pole, giving a stellar obliquity φ of near 0° . In transit, such a planet’s chord across its star’s disk would be perpendicular to the projected stellar rotation pole. In this paper, I call these “spin-orbit aligned” planets. If planets have experienced planet-planet scattering events in their past, however, they might be expected to show significant spin-orbit misalignment (Jurić & Tremaine 2008).

Rossiter-McLaughlin (R-M) measurements of the radial velocity of slowly-rotating stars during planetary transits have been highly successful at determining spin-orbit alignments. Relatively low-precision R-M measurements of spin-orbit alignment were made by Pont et al. (2009) and Moutou et al. (2009). Winn et al. (2006) and Winn et al. (2007) made early measurements of HD189733 and HD147506, showing them to be spin-orbit aligned. Johnson et al. (2008b) determined that HAT-P-1 is nearly aligned ($3.7^\circ \pm 2.1^\circ$). Narita et al. (2009) showed that HD17156 is nearly spin-orbit aligned, with a misalignment of $10^\circ \pm 5.1^\circ$. Wolf et al. (2007) determined a similarly misalignment of $12^\circ \pm 15^\circ$ in the HD149026 system, consistent with spin-orbit alignment. On the other hand, Hébrard et al. (2009) show a striking spin-orbit misalignment of $70^\circ \pm 15^\circ$ in the XO-3 planetary system. Highly precise measurements from Triaud et al. (2009) show a tiny but significant spin-orbit misalignment of $0.85^\circ \pm 0.3^\circ$ in the CoRoT-3 system. Unfortunately, Rossiter-McLaughlin measurements will likely be much more challenging rapidly-rotating stars due to their high inherent radial velocity noise.

Because more massive stars rotate much faster than the Sun, the transit lightcurves for the planets that *Kepler*

will discover around them will be qualitatively and quantitatively different from those for planets orbiting slowly-rotating stars. Russell (1939) considered this effect for eclipsing binary stars, and here I consider the effects for transiting planets. Stellar oblateness will alter the times of transit ingress and egress, and the overall transit duration, somewhat complementary to the effects of oblate planets (Barnes & Fortney 2003; Seager & Hui 2002). When the star’s spin pole and the planet’s orbit pole are aligned, the Von Zeipel effect will cause systematic errors in radius determinations for the star and the planet, and will lead to broadband color variations during transit. If the stellar spin pole and planetary orbit pole are not aligned, then bizarre transit lightcurves result that can be used to constrain both the stellar spin pole direction and the spin-orbit alignment. In this paper I investigate the effect that a fast-rotating star has on the lightcurves of transiting extra-solar planets in preparation for the results expected from *Kepler*.

2. SYNTHETIC TRANSIT LIGHTCURVES

2.1. Algorithm

In order to generate synthetic transit lightcurves with fast-rotating stars, I modified the algorithm originally developed for Barnes & Fortney (2003) and extended in Barnes & Fortney (2004) and Barnes (2007). The algorithm numerically integrates the total flux coming from the uneclipsed star, F_0 , in polar coordinates centered on the projected center of the star in the plane of the sky such that:

$$F_0 = \int_0^{R_{\text{eq}}} \int_0^{2\pi} I(r, \theta) d\theta dr \quad (1)$$

where R_{eq} is the radius of the star at its equator (see Figure 1 for a schematic of some of the geometric variables), r and θ are measured from the stellar center and counter-clockwise from the x-axis respectively, and $I(r, \theta)$ is the star’s intensity at point (r, θ) . It then evaluates the apparent stellar flux at time t , $F(t)$, relative to the out-of-transit flux F_0 , by subtracting the amount of stellar flux blocked by the planet from F_0 :

$$F_{\text{blocked}}(t) = \int_0^{R_{\text{eq}}} \int_0^{2\pi} \Gamma(r, \theta, t) I(r, \theta) d\theta dr, \quad (2)$$

and

$$F(t) = \frac{F_0 - F_{\text{blocked}}}{F_0}, \quad (3)$$

where $\Gamma(r, \theta, t) = 1$ if the planet is blocking starlight at position r , θ and time t , and $\Gamma(r, \theta, t) = 0$ if not.

The difference in the case of fast-rotating stars is that the rotation induces these stars’ equators to bulge outward. Hence the polar integral in Equations 1 and 2 no longer properly accounts for the symmetry of the problem. I quantify this effect here as the star’s oblateness, f , defined to be $f \equiv \frac{R_{\text{eq}} - R_{\text{pole}}}{R_{\text{eq}}}$ where R_{pole} is the star’s radius along the rotational pole. I assume throughout that the star’s resulting shape can be considered a MacLaurin

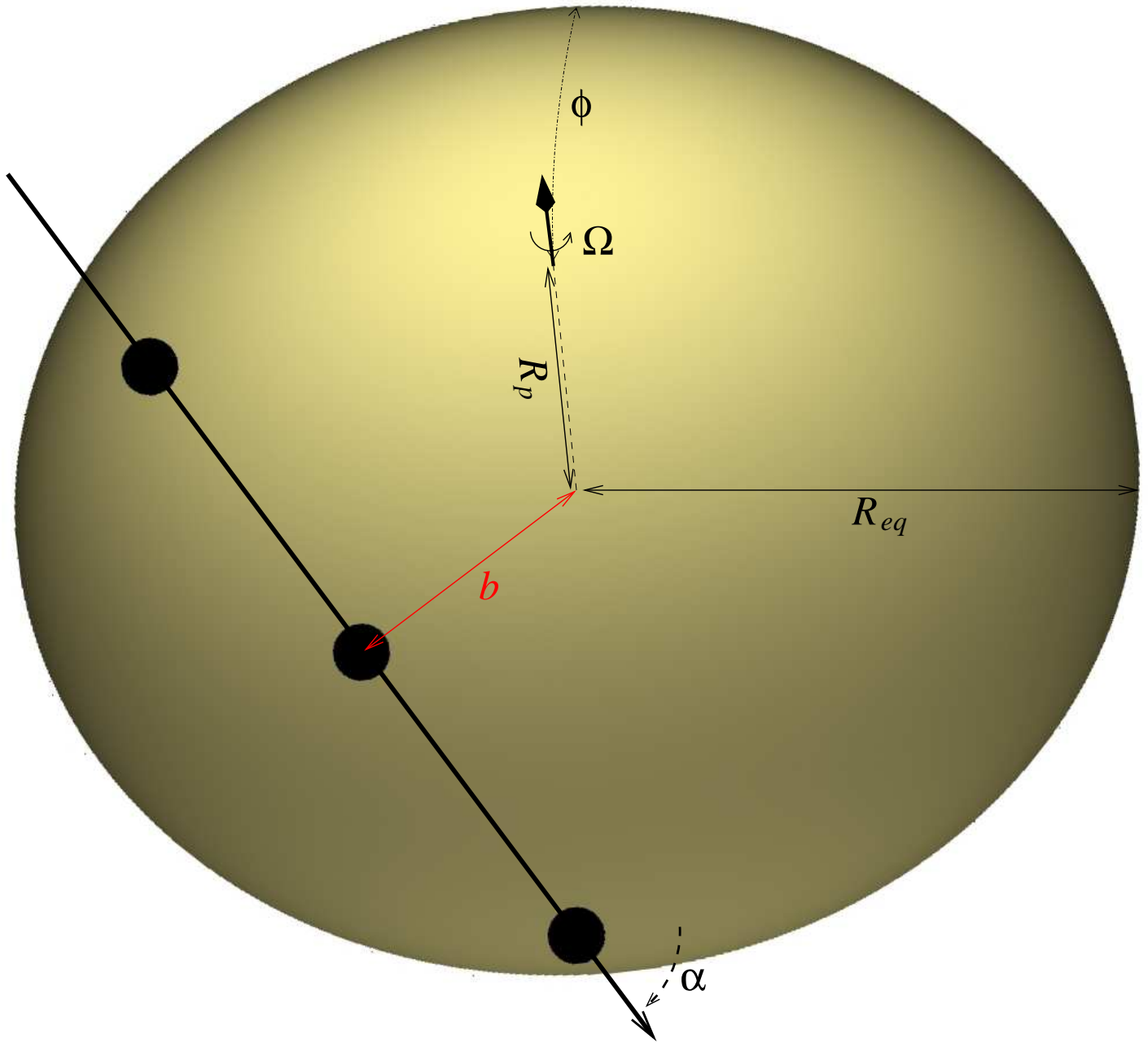


Fig. 1.— Schematic showing transit geometry along with some of the parameters referred to in the text such as: planet orbit azimuth α , transit impact parameter b , stellar obliquity φ , stellar rotation rate Ω , equatorial radius R_{eq} , and polar radius R_p .

spheroid. The value relevant for the integrals in Equations 1 and 2, though, is the effective oblateness f_{eff} , which I define to be the apparent oblateness of the star when projected into the plane of the sky. The effective oblateness is related to the actual oblateness by the stellar obliquity φ , where $\varphi = 0$ if the stellar rotation axis resides in the plane of the sky:

$$f_{\text{eff}} = 1 - \sqrt{(1-f)^2 \cos^2 \varphi + \sin^2 \varphi} . \quad (4)$$

The relationship is not a simple cosine owing to three-dimensional geometry. I will show how this expression can be derived a few paragraphs below.

With f_{eff} in hand, it becomes straightforward to incorporate the stellar asphericity. In order to avoid complex and computationally-intensive elliptical integrals, I execute a substitution for r and θ in Equations 1 and 2. I instead choose to integrate over r' and θ' , where r' and θ' are chosen so as to ‘pop’ the star into a spherical shape in r' - θ' space. To do this, I first convert the true projected r and θ measured from the star’s center into $x = r \cos \theta$ and $y = r \sin \theta$. I assume that the projected stellar rotation axis is parallel to the y -axis for simplicity – the true orientation will not be known, in general, but does not matter since it does not affect the measured stellar flux. I then let $x' = x$ and

$$y' = \frac{y}{(1-f_{\text{eff}})} , \quad (5)$$

and then set $r' = \sqrt{x'^2 + y'^2}$ and $\theta' = \text{atan2}(y', x')$ where atan2 is the C computer language arctangent function that returns a true 4-quadrant-capable angle from x and y values. The substitution in Equation 5 works equally well if you were to choose to integrate the stellar flux in cartesian xy coordinates instead of the polar integral that I use.

Equations 1 and 2 now become:

$$F_0 = (1-f_{\text{eff}}) \int_0^{R_{\text{eq}}} \int_0^{2\pi} I(r', \theta') d\theta' dr' \quad (6)$$

and

$$F_{\text{blocked}}(t) = (1-f_{\text{eff}}) \int_0^{R_{\text{eq}}} \int_0^{2\pi} \Gamma(r', \theta', t) I(r', \theta') d\theta' dr' . \quad (7)$$

The $(1-f_{\text{eff}})$ factor is introduced by the coordinate transformation: ‘popping’ the oblate star out into a circle overestimates its projected area, and hence the emitted flux, by $(1-f_{\text{eff}})^{-1}$. In the end the factor is irrelevant. When the results are plugged into Equation 3, it drops out. Hence the lightcurve generation algorithm as implemented does not use the factor $(1-f_{\text{eff}})$ explicitly at all.

All that’s left then is to determine $I(r', \theta')$ and then to integrate it. Obtaining $I(r, \theta)$ is straightforward but nontrivial. I first break out the stellar limb darkening from the normal emission, and assume blackbody radiation:

$$I(r', \theta') = B_{\lambda}(T(r', \theta')) L(r', \theta') \quad (8)$$

where $B_{\lambda}(T)$ is the blackbody function (or your desired stellar emission as a function of temperature at a given

wavelength), $T(r', \theta')$ is the temperature at a given point on the stellar disk, and $L(r', \theta')$ is the stellar limb darkening at that point. It would be possible to incorporate a more realistic stellar emission spectrum rather than to assume it to be a blackbody, but since rapidly-rotating stars are mostly of early spectral types, the differences are not significant at the level of the present investigation.

A modified version of the Von Zeipel theorem (von Zeipel 1924) determines the stellar temperature T at every point. The temperature on the surface of a rapidly rotating star is given by (Maeder 2009)

$$T = T_{\text{pole}} \frac{g^{\beta}}{g_{\text{pole}}^{\beta}} \quad (9)$$

where g is the magnitude of the local effective surface gravity and T_{pole} and g_{pole} are the pole’s temperature and surface gravity, respectively. The value β is known as the gravity-darkening parameter. Its nominal value is 0.25 for a purely radiative star, as derived by von Zeipel; for our numerical calculations I use an empirically measured β , as detailed below. The local surface gravity vector \vec{g} has two terms: one Newtonian, and one centrifugal:

$$\vec{g} = -\frac{GM_*}{R^2} \hat{r} + \Omega^2 R_{\perp} \hat{r}_{\perp} \quad (10)$$

where G is the universal gravitational constant, M_* is the stellar mass, Ω is the stellar rotation rate in radians per second, R is the distance from the star center to the point in question, and R_{\perp} is the distance from the star’s rotation axis to the point in question. The two hatted symbols, \hat{r} and \hat{r}_{\perp} are unit vectors pointing to the point in question from the stellar center and stellar rotation axis respectively.

So, then, to know I you need to know g , and to know g you need to know the three-dimensional vector position of each point that you see on the star. In this case you already know r' and θ' , from which you can trivially derive x and y , the location of 2-d projection in the plane of the sky of the point of interest with respect to the center of the star. What is left then is to determine z . This is nontrivial.

The geometrical constraint on z is that its value must conform to the surface of an oblate spheroid given x , y , the stellar radius R_{eq} , and the oblateness f . This is easy enough when the stellar obliquity is zero, and thus when the y -axis is parallel to the stellar rotation axis. So I define a new set of coordinate axes with the same origin as the x - y - z system, at the center of the star. However this new system is rotated in the y - z plane (*i.e.* around the x -axis) by an angle φ , the star’s obliquity to the plane of the sky. Call this the x_0, y_0, z_0 system, where

$$\begin{aligned} x_0 &\equiv x , \\ y_0 &\equiv y \cos(\varphi) + z \sin(\varphi) , \text{ and} \\ z_0 &\equiv -y \sin(\varphi) + z \cos(\varphi) . \end{aligned} \quad (11)$$

In this new obliquity-rotated coordinate system, the surface of the star’s photosphere follows

$$x_0^2 + \frac{y_0^2}{(1-f)^2} + z_0^2 = R_{\text{eq}}^2 . \quad (12)$$

Plugging the definitions of x_0 , y_0 , and z_0 from Equations 11 into Equation 12, I solve for z in terms of a known x and y . The solution to the resulting quadratic is

$$z = \frac{-2y(1 - (1 - f)^2) \sin \varphi \cos \varphi + \sqrt{d}}{2((1 - f)^2 \cos^2 \varphi + \sin^2 \varphi)} \quad (13)$$

where the determinant d is

$$d \equiv 4y^2(1 - (1 - f^2))^2 \sin^2 \varphi \cos^2 \varphi + \\ -4((\cos^2 \varphi(1 - f)^2 + \sin^2 \varphi) \times \\ ((y^2 \sin^2 \varphi - R_{\text{eq}}^2 + x^2)(1 - f^2) + y^2 \cos^2 \varphi)) . \quad (14)$$

I choose the positive root of the determinant as the negative root represents the invisible second interception of the line-of-sight with the photosphere that occurs on the back side of the star as seen from Earth. Equation 4 above can be derived by setting the determinant d equal to zero to establish the outer edge of the star's disk as seen from Earth, and then solving for the proper f_{eff} to reproduce that disk.

I now have all of the necessary parameters to compute the flux coming from each point on the star. To do so, at each x , y point use Equation 13 to get z , and then plug z into Equations 11 to get x_0 , y_0 , and z_0 . Do the vector addition to get \vec{g} from Equation 10 in x_0 , y_0 , z_0 space where

$$\vec{R} \equiv \frac{x_0}{R} \hat{i}_0 + \frac{y_0}{R} \hat{j}_0 + \frac{z_0}{R} \hat{k}_0 \quad , \\ \vec{R}_{\perp} \equiv \frac{x_0}{R_{\perp}} \hat{i}_0 + \frac{z_0}{R_{\perp}} \hat{k}_0 \quad , \\ R \equiv \sqrt{x_0^2 + y_0^2 + z_0^2} \\ R_{\perp} \equiv \sqrt{x_0^2 + z_0^2}$$

Then plug $g \equiv |\vec{g}|$ into Von Zeipel's Equation (Equation 9) to get T , and then derive a flux from T using a blackbody curve or your choice of a more sophisticated emitted flux.

2.2. Parameters

In order to generate appropriate and representative lightcurves that can be used for comparison to transits yet undiscovered, I calculate all transit lightcurves as if the parent star were Altair (α Aquilae). The true host stars for *Kepler*-detected transiting planets will show varying stellar masses, polar temperatures, radii, and rotation rates. I elect to use Altair because I think that its spectral type (A7V) is broadly representative of the majority of the expected fast-rotating stars in the *Kepler* sample, and because its parameters are well-characterized by interferometric imaging (Monnier et al. 2007). Not all sets of parameters produce physically plausible stars; I avoid non-physical combinations by only using this one set of known stellar values.

The specific stellar parameters that I use are $M_* = 1.8 M_{\odot}$ (Peterson et al. 2006a), $R_{\text{eq}} = 2.029 R_{\odot}$, $T_{\text{pole}} = 8450$ K, $\beta = 0.190$, $f = 0.1947$, and a stellar rotation period of 8.64 hours (all as directly measured for Altair by

Monnier et al. 2007). For the planet, I assume $R_p = R_{\text{Jup}}$ and an orbit semimajor axis of 0.05 AU (corresponding to a period of 3.04 days) for familiarity with the lightcurves of known transiting hot Jupiters. Transit lightcurve shapes are invariant with orbit period; only the timescale changes. Hence the curves that I show here can be converted for different-period planets by stretching the x-axis.

In fitting I adjust for the c_1 and c_2 limb darkening coefficients outlined in Brown et al. (2001). I generate the synthetic lightcurves using $c_1 = 0.640$ and $c_2 = 0.0$. I also assume a monochromatic observation at 0.51 microns wavelength except where otherwise noted.

3. SPIN-ORBIT ALIGNED

I show synthetic transit lightcurves of planets in spin-orbit aligned geometries in Figure 2, for various transit impact parameters b . The lightcurves are symmetrical. Furthermore, since the parts of the star that the planet transit chord passes over all have the same temperature because they equidistant from the stellar rotation pole, the transit bottom shows normal limb-darkening curvature. As a result, the specific lightcurve shapes for spin-orbit aligned transiting planets are indistinguishable from those for planets orbiting spherical, slow-rotating stars.

The transit depths and durations are different, though. In particular, the transit depth *increases* with impact parameter, opposite of the case for spherical stars. If you were to fit these lightcurves assuming a spherical star, then the resulting best-fit transit parameters would be different from the actual ones. In order to show this effect, I fit the synthetic transit lightcurves show in Figure 2 using a Leavenberg-Marquardt chi-squared minimization scheme from Press et al. (1992) as described in Barnes & Fortney (2003) and show the resulting best-fit parameters in Table 1.

For planets transiting across the center of the star ($b = 0.0$), the best-fit parameters retain easily-interpreted astrophysical meaning. The ratio of radii R_p/R_* comes from the total transit depth, which in this case is nearly identical to that for the case of a $b = 0.0$ transit across a spherical star with radius equal to the equatorial radius of the fast-rotating star. In that case, while using the Altair parameters that I use here, the total larger projected area of the stellar disk makes up for lower flux coming from the polar regions, yielding similar net stellar flux. The fitting algorithm thus gets R_p/R_* correct, assuming $R_* = R_{\text{eq}}$ and not the real average radius of the projected disk, $(1 - \frac{f}{2})R_{\text{eq}}$. The total duration of the transit and the duration of ingress and egress fix the impact parameter, which the fit correctly determines to be near 0.0 ($i \sim 90^\circ$), and the stellar radius, which is very close to the star's true equatorial radius. Hence the planetary radius also comes out correctly. Limb darkening is right because of the same-temperature effect described above.

As I consider higher and higher impact parameters, shown in Figure 2 as fractions of Altair's polar radius

TABLE 1

BEST-FIT TRANSIT PARAMETERS ASSUMING SPHERICAL STAR FOR VARIOUS TRANSIT GEOMETRIES.

Stellar Obliquity (φ , $^\circ$)	Planet's Azimuth (α , $^\circ$)	Transit Impact Parameter (b , R_{pole})	Best- fit R_* R_\odot	R_p R_{Jup}	Parameters Inclination (i , $^\circ$)	Limb Dark 1 c_1	Limb Dark 2 c_2
0 $^\circ$	0 $^\circ$	0.0 R_{pole}	2.050 R_\odot	0.999 R_{Jup}	88.23 $^\circ$	0.612	
0 $^\circ$	0 $^\circ$	0.3 R_{pole}	2.014 R_\odot	1.034 R_{Jup}	86.95 $^\circ$	0.621	
0 $^\circ$	0 $^\circ$	0.6 R_{pole}	1.970 R_\odot	1.141 R_{Jup}	84.07 $^\circ$	0.626	
0 $^\circ$	0 $^\circ$	0.9 R_{pole}	1.937 R_\odot	1.291 R_{Jup}	80.94 $^\circ$	0.582	
30 $^\circ$	0 $^\circ$	-0.9 R_{pole}	1.91 R_\odot	1.27 R_{Jup}	81.70 $^\circ$	0.826	1.000 *
30 $^\circ$	0 $^\circ$	-0.6 R_{pole}	2.02 R_\odot	1.24 R_{Jup}	84.01 $^\circ$	0.834	1.000 *
30 $^\circ$	0 $^\circ$	-0.3 R_{pole}	2.08 R_\odot	1.16 R_{Jup}	85.93 $^\circ$	0.805	1.000 *
30 $^\circ$	0 $^\circ$	0.0 R_{pole}	2.04 R_\odot	1.02 R_{Jup}	88.70 $^\circ$	0.723	1.000
30 $^\circ$	0 $^\circ$	0.3 R_{pole}	2.02 R_\odot	1.01 R_{Jup}	89.97 $^\circ$	0.726	0.859
30 $^\circ$	0 $^\circ$	0.6 R_{pole}	2.123 R_\odot	0.987 R_{Jup}	83.05 $^\circ$	0.465	
30 $^\circ$	0 $^\circ$	0.9 R_{pole}	2.143 R_\odot	1.059 R_{Jup}	80.19 $^\circ$	0.268	
90 $^\circ$	0 $^\circ$	0.0 R_{pole}	2.30 R_\odot	1.17 R_{Jup}	80.30 $^\circ$	0.916	1.000 *
90 $^\circ$	0 $^\circ$	0.3 R_{pole}	2.06 R_\odot	1.00 R_{Jup}	84.63 $^\circ$	1.000	1.000 *
90 $^\circ$	0 $^\circ$	0.6 R_{pole}	2.05 R_\odot	1.01 R_{Jup}	87.10 $^\circ$	1.000	1.000 *
90 $^\circ$	0 $^\circ$	0.9 R_{pole}	2.04 R_\odot	1.01 R_{Jup}	89.47 $^\circ$	1.000	1.000 *
0 $^\circ$	90 $^\circ$	0.0 R_{pole}	1.89 R_\odot	1.12 R_{Jup}	84.57 $^\circ$	-1.000	-1.000 *
0 $^\circ$	90 $^\circ$	0.3 R_{pole}	1.91 R_\odot	1.11 R_{Jup}	84.00 $^\circ$	-1.000	-1.000 *
0 $^\circ$	90 $^\circ$	0.6 R_{pole}	1.92 R_\odot	1.04 R_{Jup}	82.94 $^\circ$	-1.000	-1.000 *
0 $^\circ$	90 $^\circ$	0.9 R_{pole}	1.85 R_\odot	0.91 R_{Jup}	82.12 $^\circ$	-0.585	-1.000 *

NOTE.—Tabled here are the best-fit parameters R_* , R_p , i , c_1 , and c_2 for fits assuming spherical stars of synthetic lightcurves of hypothetical Altair-planet systems with $R_p = R_{\text{Jup}}$ and the planet at 0.05 AU. The stellar obliquity to the plane of the sky φ for each synthetic curve is listed at left, followed by the angle α between the planet's orbit pole and the stellar rotation axis projected into the plane of the sky. When fixing c_2 at zero and fitting only for c_1 resulted in a high-quality fit to the data, c_2 is not listed. Fits that have a '*' next to their value for c_2 did not produce good fits even with the second limb darkening parameter.

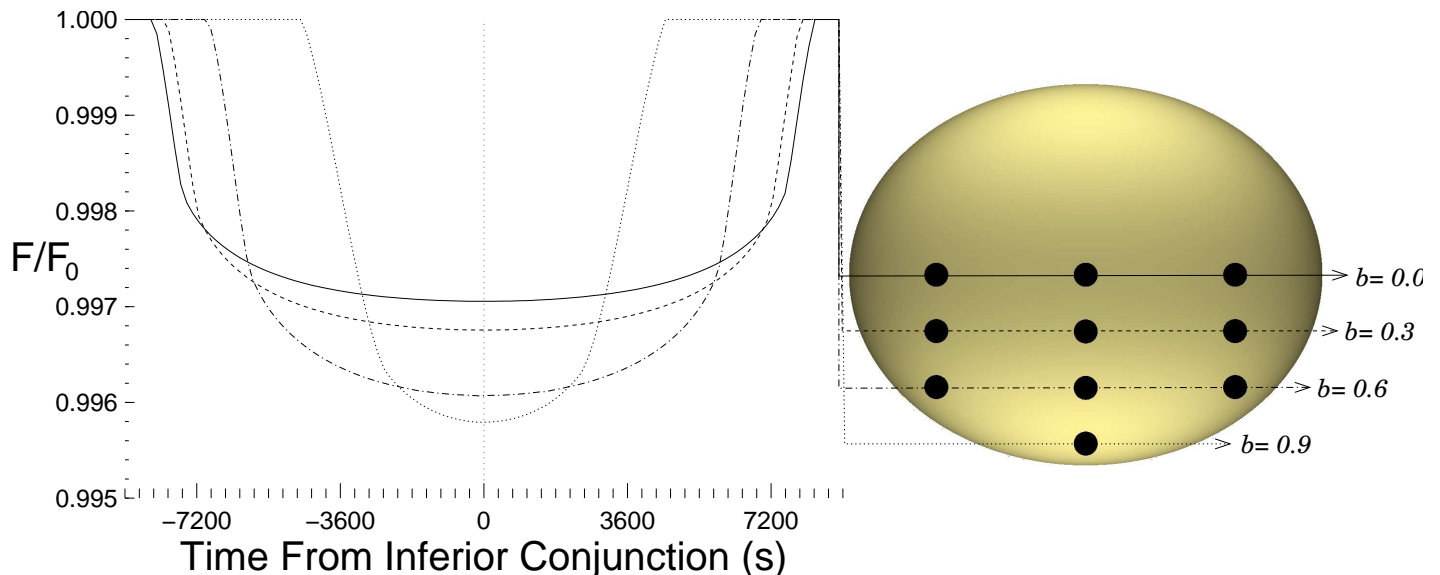


Fig. 2.— Synthetic lightcurves for transiting $1 R_{Jup}$ in a spin-orbit aligned 0.05 AU orbit around an Altair-like star are plotted. The four curves correspond to planets with transit impact parameters of $b = 0.0 R_{pole}$ (solid), $b = 0.3 R_{pole}$ (dashed), $b = 0.6 R_{pole}$ (dot-dashed), and $b = 0.9 R_{pole}$ (dotted). The curves’ shapes are indistinguishable from transits of slow-rotating, spherical stars using different parameters. Transits nearer to the pole are deeper because the stellar photosphere is hotter there due to the Van Zeipel effect.

$1.63 R_{\odot}$, the best-fit parameters deviate further and further from the actual values. As the planet transits across hotter, brighter parts of the stellar photosphere near the pole, the best-fit value for planet radius increases by up to 30% above the input planet radius. The stellar radius, driven by the somewhat longer transit durations, drops slightly but stays closer to the input star’s equatorial radius than it does to the true average radius of the stellar disk. Less importantly, the inclination and limb darkening parameter are somewhat underestimated.

The end result of these calculations is that if the planets orbiting fast-rotating stars are spin-orbit aligned, it may not be evident at first glance. The transit lightcurves will not stick out. Instead the measured transit parameters’ errors will be systematic in nature, and the fits will still be good.

If the spin-orbit aligned planet case turns out to be prevalent around fast-rotating stars in the *Kepler* sample, then measuring the spin-orbit alignment for planets will require a separate identification of the star’s fast-rotating status. *Kepler*’s photometric precision should be good enough to identify the star’s rotation rate in long time-series photometry. If the planets transiting those stars show normal-looking lightcurves, that would indicate that the planet is spin-orbit aligned. If most or all planets are spin-orbit aligned, then they likely either formed in-situ or migrated there, and were not scattered by close encounters with other planets.

4. SPIN-ORBIT MISALIGNED

If instead the transiting planets around fast-rotating stars experienced close encounters that threw them out

of spin-aligned orbits, then more exotic lightcurves result. Recent Rossiter-McLaughlin results from transiting planetary systems indicate that this situation may be more common than previously thought (Hébrard et al. 2009). Given the difficulty of radial velocity, and thus Rossiter-McLaughlin, measurements around early-type stars, transit photometry may then be the best way to measure the spin-orbit alignment in those systems.

4.1. SYMMETRIC

Just because the transit lightcurve of a planet around a fast-rotating star is symmetric does not mean that the planet is spin-orbit aligned. Any planet whose transit chord is perpendicular to the projected stellar rotation pole, *i.e.* for which the angle between the transit chord and the projected pole, α , is 0.0° , will show a symmetric lightcurve. I plot the lightcurve for a few such hypothetical planets in Figures 3 and 4. Figure 3 shows planets around a star with obliquity $\varphi = 30^{\circ}$. Figure 4 shows transits for a star viewed pole-on with $\varphi = 90^{\circ}$.

Although these lightcurves are symmetrical about the mid-transit point, unlike the spin-aligned case they are not well-fit using a model that assumes a spherical star. In the $\varphi = 30^{\circ}$ case the stellar obliquity removes the symmetry in the stellar disk, thereby making transits toward the north and south poles distinct from one another. I arbitrarily choose to define those transits toward the north of the center of the stellar disk to have a negative impact parameter so as to differentiate the two possible cases.

In the positive impact parameter cases in Figure 3, the planet crosses the cooler equatorial regions of the star. Hence those transits are relatively shallow. The geom-

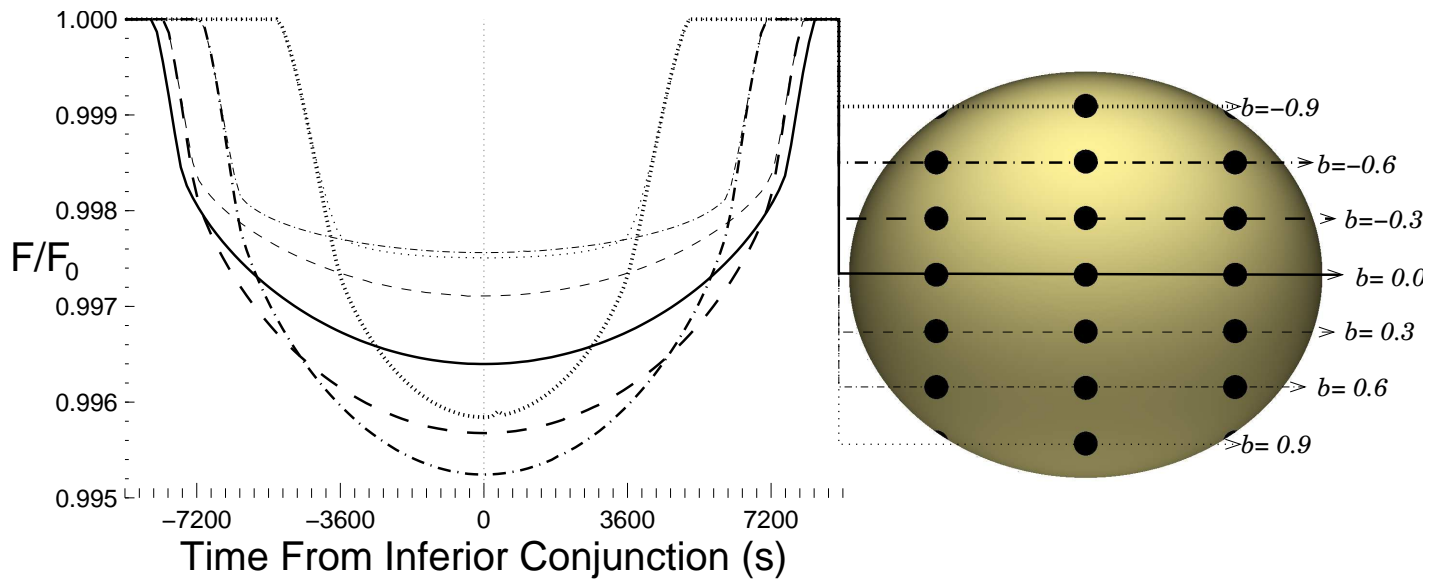


Fig. 3.— Synthetic lightcurves for transiting $1 R_{Jup}$ in a 0.05 AU orbit around an Altair-like star with obliquity 30° are plotted. The seven curves correspond to planets with transit impact parameters of $b = -0.9 R_{pole}$ (thick dotted), $b = -0.6 R_{pole}$ (thick dot-dashed), $b = -0.3 R_{pole}$ (thick dashed), $b = 0.0 R_{pole}$ (thick solid), $b = 0.3 R_{pole}$ (dashed), $b = 0.6 R_{pole}$ (dot-dashed), and $b = 0.9 R_{pole}$ (dotted). The curves' shapes start to differ from those of transits of slow-rotating, spherical stars. The ingress and egress of transits at opposite impact parameter are nearly the same. The transit bottoms differ. Transits near the hot stellar north pole are deep and show severe curvature of the transit bottom.

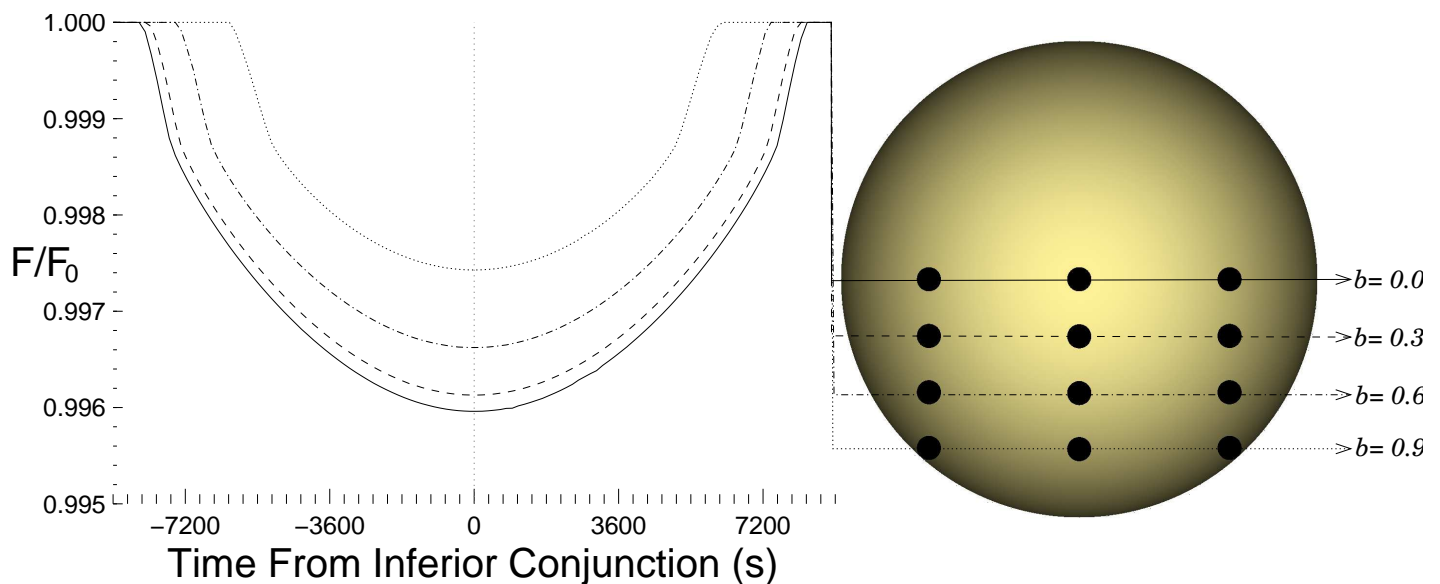


Fig. 4.— Synthetic lightcurves for transiting $1 R_{Jup}$ in a 0.05 AU orbit around an Altair-like star with obliquity 90° (pole-on) are plotted. The four curves correspond to planets with transit impact parameters of $b = 0.0 R_{pole}$ (solid), $b = 0.3 R_{pole}$ (dashed), $b = 0.6 R_{pole}$ (dot-dashed), and $b = 0.9 R_{pole}$ (dotted). The lightcurves show a pronounced ‘U’-shape that is typically considered to be characteristic of grazing eclipsing binary stars rather than planets. The extreme curvature of the usually flat planet transit bottom makes the locations of second and third contact difficult to discern. Due to symmetry around the stellar pole, all transits with these same impact parameters will look the same regardless of α .

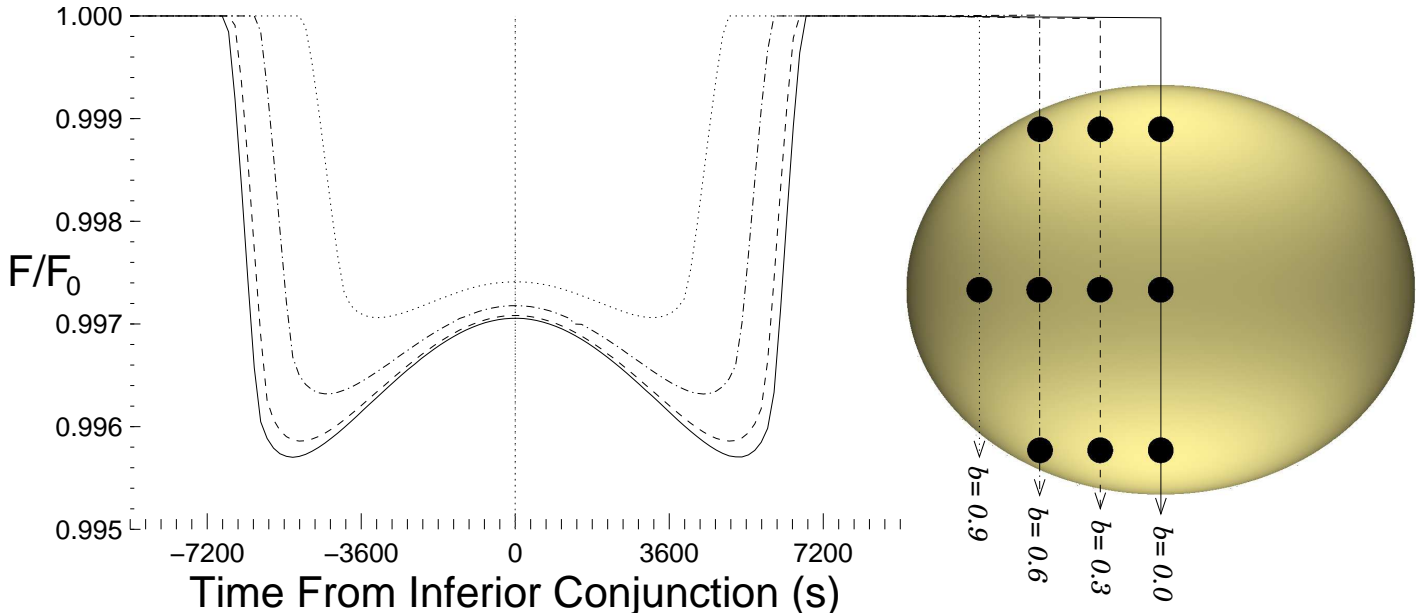


Fig. 5.— Synthetic lightcurves for transiting $1 R_{\text{Jup}}$ in a 0.05 AU orbit around an Altair-like star with obliquity 0° (equator-on) are plotted, similar to Figure 2, but this time with an azimuthal angle of $\alpha = 90^\circ$. The four curves correspond to planets with transit impact parameters of $b = 0.0 R_{\text{pole}}$ (solid), $b = 0.3 R_{\text{pole}}$ (dashed), $b = 0.6 R_{\text{pole}}$ (dot-dashed), and $b = 0.9 R_{\text{pole}}$ (dotted). This unlikely 90° transit geometry also produces symmetric transit lightcurves, albeit highly unusual ones. These curves are deepest near second and third contact, and shallow at mid-transit. If assuming a spherical-star model, then the interpretation of this “double-horned” structure might be a negative limb-darkening coefficient possibly associated with a temperature inversion in the stellar atmosphere; however, such a model fits these data very poorly (see text).

etry of the orthographic projection of the star as seen from Earth means that for the high impact parameter, $b = 0.6 R_{\text{pole}}$ and $b = 0.9 R_{\text{pole}}$ cases, the planet covers more southerly stellar latitudes at ingress and egress than it does at mid-transit. Because those more southerly latitudes are hotter, the net result is a flatter lightcurve bottom than occurs for spherical stars with the same limb darkening parameter ($c_1 = 0.640$). The flatness appears as a lower limb darkening parameter c_1 in Table 1. For the $b = 0.6 R_{\text{pole}}$ and $b = 0.9 R_{\text{pole}}$ cases the model overestimates the star’s radius; the best-fit radius is greater than even the star’s equatorial radius.

For $b = 0.0 R_{\text{pole}}$ and $b = 0.3 R_{\text{pole}}$ in the $\varphi = 30^\circ$ case, the planet transits closer to the star’s north pole, and hence the transit depth becomes progressively greater. The ingress and egress are again at more southerly latitudes than mid-transit. But now mid-transit is north of the equator, so the ingress and egress are cooler than mid-transit, enhancing the curvature of the lightcurve bottom. I was unable to find satisfactory fits to either of these synthetic lightcurves using just the first Brown et al. (2001) limb darkening coefficient c_1 alone, even though it was the only one used to generate the synthetic lightcurve. However, by allowing the fitting algorithm to optimize c_2 as well I managed to find reasonable fits for $b = 0.0 R_{\text{pole}}$ and $b = 0.3 R_{\text{pole}}$.

When fitting $b = -0.3 R_{\text{pole}}$, $b = -0.6 R_{\text{pole}}$, and $b = -0.9 R_{\text{pole}}$ not even two-limb-darkening fits were acceptable. The curvature on these transits is so extreme that even though they are symmetric, they are discern-

able from reasonable spherical-star models because of the severity of their curvature. In fact, the curvature of these planets’ transit bottoms are so severe that the lightcurves look ‘V’-shaped instead of ‘U’-shaped. The transit bottom is difficult to discern. The resulting rounded shape might be mistaken for an eclipsing binary star.

Fits for transits of pole-on oriented fast-rotating stars are similar. As shown in Figure 4, the center of the stellar disk is particularly bright relative to the limb owing to the center being the hot pole and the limb being the cool equator. Thus here again the curvature of the transit lightcurve between second and third contacts is large, and cannot be satisfactorily fit by a spherical-star model. In both these cases the difficulty in identifying these type of planetary transits in the *Kepler* data will probably be recognizing that they are not eclipsing binaries, not in thinking that they are planets around spherical stars.

An observer would also measure a symmetrical transit lightcurve if a planet orbits a zero obliquity ($\varphi = 0.0^\circ$) star such that its orbit plane contains the stellar rotation pole, *i.e.* with $\alpha = 90^\circ$. I show synthetic lightcurves for such a situation in Figure 5. These are strange transits. By moving parallel to the star’s orbit pole, the planets first encounter the limb-darkened edge of the star. Shortly after second contact, they cover the brightest part of the stellar photosphere underneath the transit chord. The lightcurve is deepest there. Over the equator at mid-transit the transit depth is shallow, and then the process repeats itself backwards on egress.

The resulting lightcurve has a “double-horned” structure that bears a resemblance to what a transit across a limb-brightened star would look like. However, spherical-star model fits cannot reproduce the specific structure. In particular, a limb-brightened star would have sharp points at second and third contacts where the derivative is discontinuous and changes sign. The fast-rotating star $\varphi = 0^\circ$ $\alpha = 90^\circ$ transits in Figure 5 instead have rounded horns at second and third contact owing to the combination of limb- and gravity-darkening. The resulting rounded double-horn shape is both characteristic and diagnostic of this kind of transit.

4.2. ASYMMETRIC

If the stellar orientation and transit chord have more exotic geometries, then highly unusual asymmetric lightcurves result. A star with obliquity $\varphi = 30^\circ$ and transit chord azimuth $\alpha = 90^\circ$ (motion parallel to the projected stellar rotation axis) presents an easy such case to visualize (Figure 6). Because the stellar disk presents only a left-right symmetry, these transits pass over very different photospheric temperatures in the first half of the transit relative to the second half.

In the $\varphi = 30^\circ$, $\alpha = 90^\circ$, impact parameter $b = 0.0 R_{\text{pole}}$ case, the planet first crosses a darkened stellar limb before occulting the star’s hot north pole. The resulting lightcurve is deepest at this point. After mid-transit the planet occults the cool equator for a shallower transit depth, but then the depth increases again near third contact as the planet covers higher southern latitudes near the southern stellar limb. The same process occurs in a more abbreviated fashion as the impact parameter b increases.

If the transit chord azimuth is oblique, then the lightcurves can become quite complex as shown in Figure 7. The central $b = 0.0 R_{\text{pole}}$ transit resembles those from Figure 6. The more northerly transits (those defined to have negative impact parameters) also show strong lightcurve asymmetries, with deep first halves and shallowing second halves. Some of the lightcurves turn over again near third contact, but the ones with more negative impact parameters do not.

For positive, more southerly impact parameters, the depth asymmetry decreases. Further from the hot pole the temperatures under the transit chord are more uniform. The $b = 0.9 R_{\text{pole}}$ transit is particularly interesting. It shows a nearly uniform depth in time, but while the ingress is long and gently curving, the egress is abrupt. A higher photometric precision would be required to definitively identify such a transit lightcurve as being one from a fast-rotating star than would be necessary for some of the more spectacularly asymmetric lightcurves.

With oblique azimuths also come uncentered lightcurves. Because of the stellar oblateness, the center of these transits does not occur at the time of the planet’s inferior conjunction, that is, when the planet is closest to the Earth. The total discrepancy can be up to a few tenths of the

total transit duration, depending on the stellar oblateness and the transit geometry.

The oblique azimuth transits of fast-rotating stars also introduce an asymmetry in the duration of transit ingress and egress. This effect comes about because the angle between the stellar limb and the transit chord is different on ingress and egress, thereby causing the transiting planet to take different amounts of time to cross the limb in each case.

Lightcurve asymmetries can occur in zero-obliquity ($\varphi = 0^\circ$) stars as well when the transit chord azimuth is oblique. I show such a case in Figure 8, with $\varphi = 0^\circ$ and $\alpha = 60^\circ$. The central $b = 0.0 R_{\text{pole}}$ transit is symmetric, similar to those from Figure 5. Non-central transits are asymmetric and resemble those from Figure 6 with one half of the transit being deeper than the other. In this $\varphi = 0^\circ$ oblique case, the transits with negative impact parameter are the time-inverse of those with positive impact parameter.

5. COLOR EFFECTS

Due to the temperature nonuniformity across the stellar disk, transit lightcurves around rapidly-rotating stars differ as a function of wavelength. I show an example of this effect in Figure 9. While a hotter blackbody radiates more flux at all wavelengths than a colder one, the flux ratio (hotter over colder) is greater at the Wien end of the blackbody curve. Hence the effects of rapid rotation in transit lightcurves are maximized at short wavelengths.

At wavelengths much longer than the blackbody emission peak, the flux ratio between the hotter and colder areas approaches the temperature ratio in Kelvin. Utilizing multiple wavelength lightcurve observations would strongly constrain the temperature structure on the stellar disk in addition to the transit parameters. This effect will be important when fitting for a fully-consistent model for the star (instead of assuming Altair’s parameters as I do in this paper).

6. CONCLUSION

The gravity-darkening effect for rapidly rotating, oblate stars first predicted by von Zeipel (1924) allows for highly unusual lightcurves when such a star is transited by an extrasolar planet. The distinctive lightcurves allow for a solely photometric determination of the relative alignment between the stellar spin axis and the planet’s orbit normal (spin-orbit alignment), a measurement that usually requires radial velocity measurements of the Rossiter-McLaughlin effect. The alignment bears a fingerprint of the planet’s formation and evolution. Planets that form in an orderly fashion and migrate within a disk ought to end up coplanar with the stellar equator. Those that have experienced planet-planet scattering events ought in general to not be spin-orbit aligned.

Spin-orbit aligned planets around fast-rotating stars

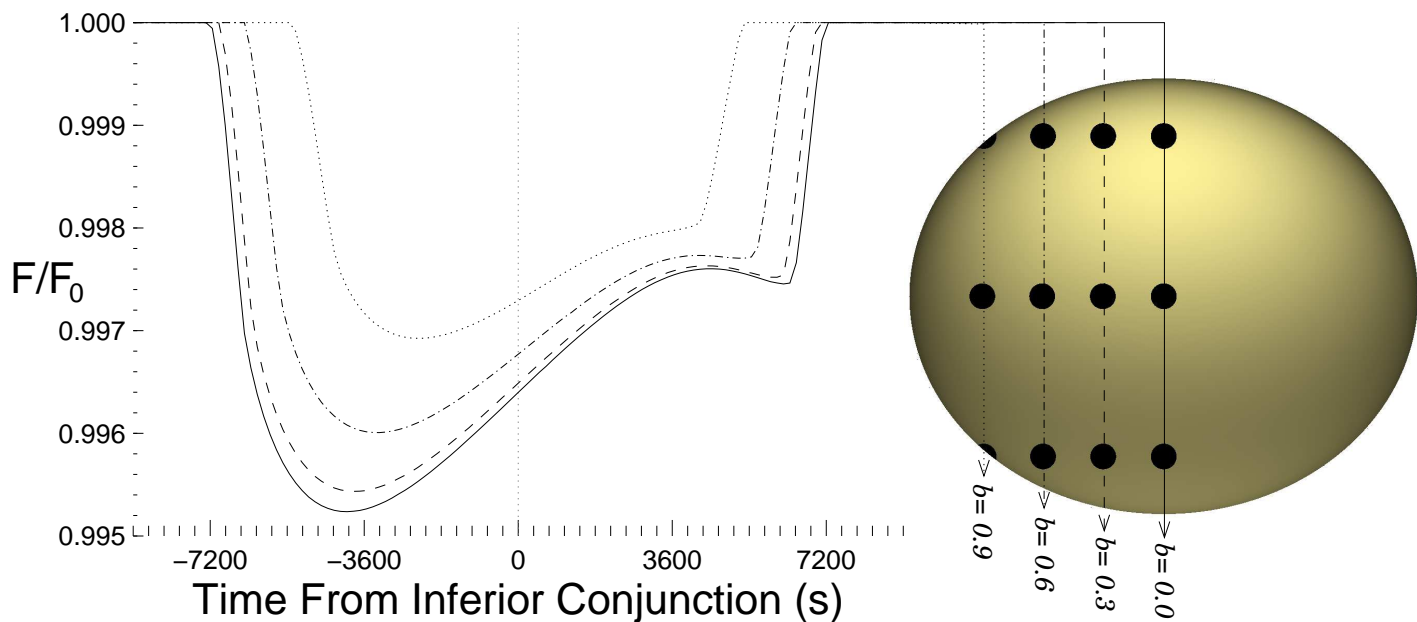


Fig. 6.— Synthetic lightcurves for transiting $1 R_{\text{Jup}}$ in a 0.05 AU orbit around an Altair-like star with obliquity 30° are plotted, similar to Figure 3, but this time with an azimuthal angle of $\alpha = 90^\circ$. The four curves correspond to planets with transit impact parameters of $b = 0.0 R_{\text{pole}}$ (solid), $b = 0.3 R_{\text{pole}}$ (dashed), $b = 0.6 R_{\text{pole}}$ (dot-dashed), and $b = 0.9 R_{\text{pole}}$ (dotted). The resulting lightcurves are highly asymmetric, being deeper on the side of the lightcurve where the planet passes over the hot northern stellar pole.

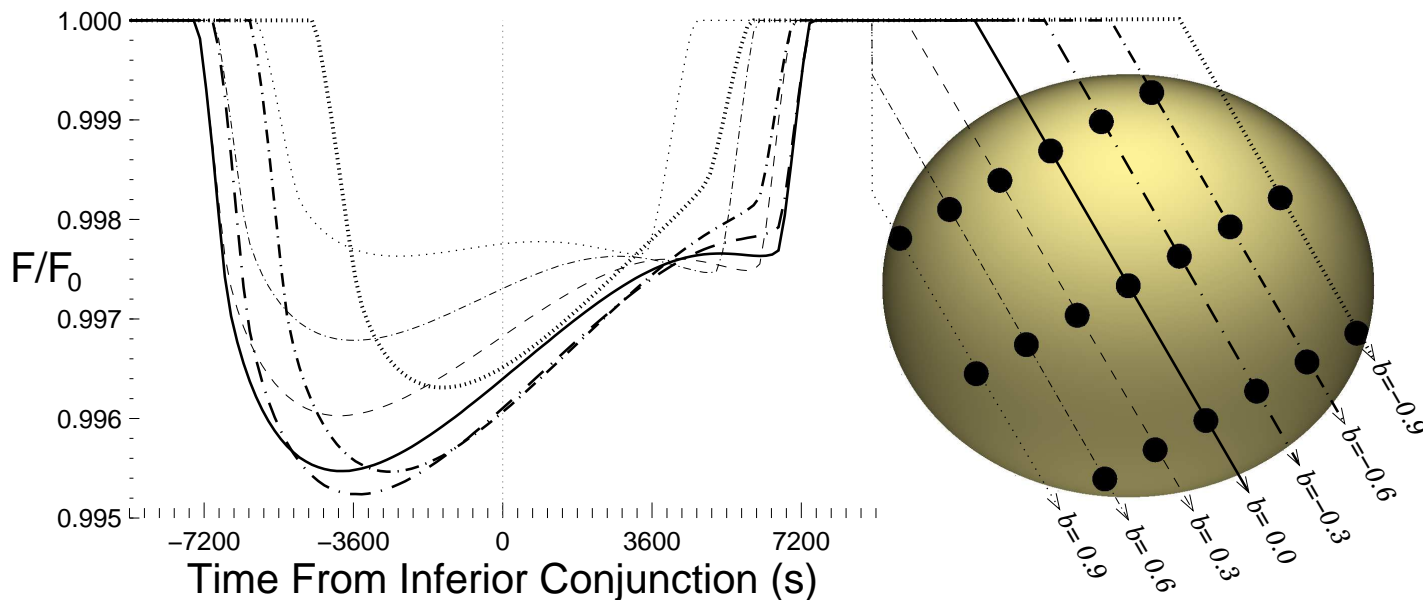


Fig. 7.— Synthetic lightcurves for transiting $1 R_{\text{Jup}}$ in a 0.05 AU orbit around an Altair-like star with obliquity 30° are plotted, similar to Figure 3 but an azimuthal angle of $\alpha = 60^\circ$. The seven curves correspond to planets with transit impact parameters of $b = -0.9 R_{\text{pole}}$ (thick dotted), $b = -0.6 R_{\text{pole}}$ (thick dot-dashed), $b = -0.3 R_{\text{pole}}$ (thick dashed), $b = 0.0 R_{\text{pole}}$ (thick solid), $b = 0.3 R_{\text{pole}}$ (dashed), $b = 0.6 R_{\text{pole}}$ (dot-dashed), and $b = 0.9 R_{\text{pole}}$ (dotted). With this oblique azimuth, the photometric lightcurve center does not correspond with the point where the planet is nearest to Earth. The lightcurves show a diversity of complex asymmetric shapes as a function of impact parameter.

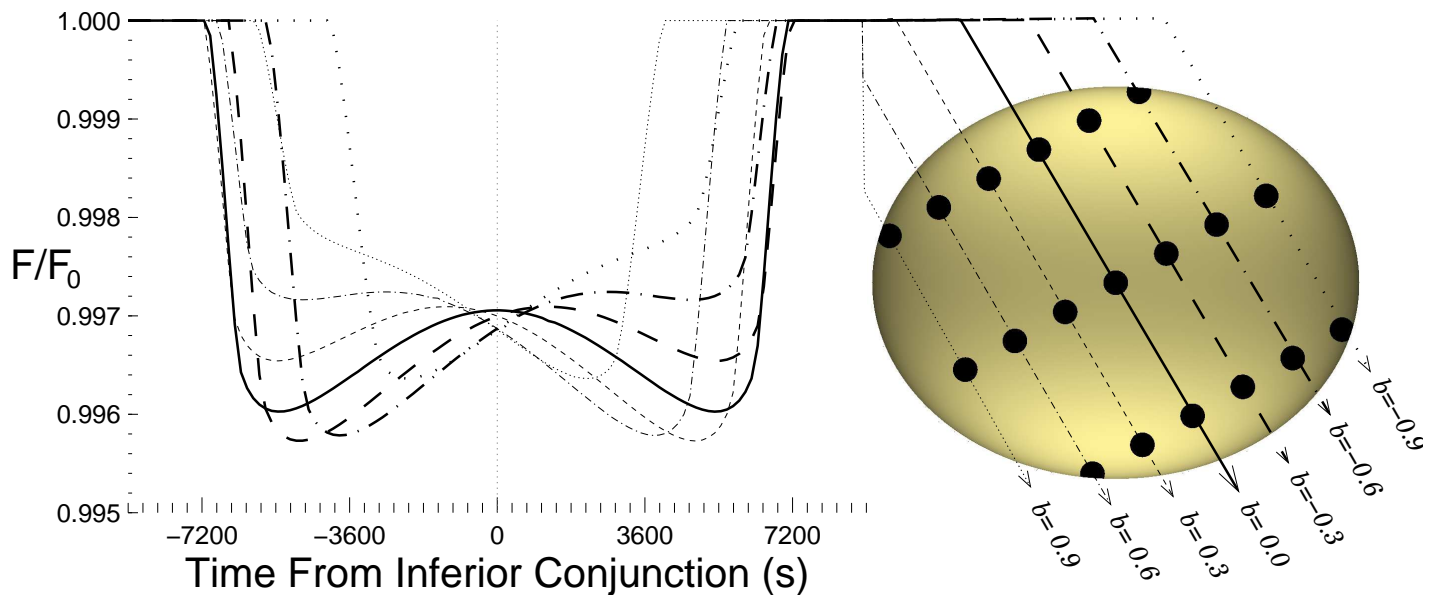


Fig. 8.— Synthetic lightcurves for transiting $1 R_{\text{Jup}}$ in a 0.05 AU orbit around an Altair-like star are plotted, similar to Figure 7 but with an obliquity $\varphi = 0^\circ$. The seven curves correspond to planets with transit impact parameters of $b = -0.9 R_{\text{pole}}$ (thick dotted), $b = -0.6 R_{\text{pole}}$ (thick dot-dashed), $b = -0.3 R_{\text{pole}}$ (thick dashed), $b = 0.0 R_{\text{pole}}$ (thick solid), $b = 0.3 R_{\text{pole}}$ (dashed), $b = 0.6 R_{\text{pole}}$ (dot-dashed), and $b = 0.9 R_{\text{pole}}$ (dotted). Due to the symmetry of the stellar disk in this case the $b = 0.0 R_{\text{pole}}$ case shows a symmetric lightcurve, and positive impact parameters have time-reversed lightcurves when compared to their negative counterparts.

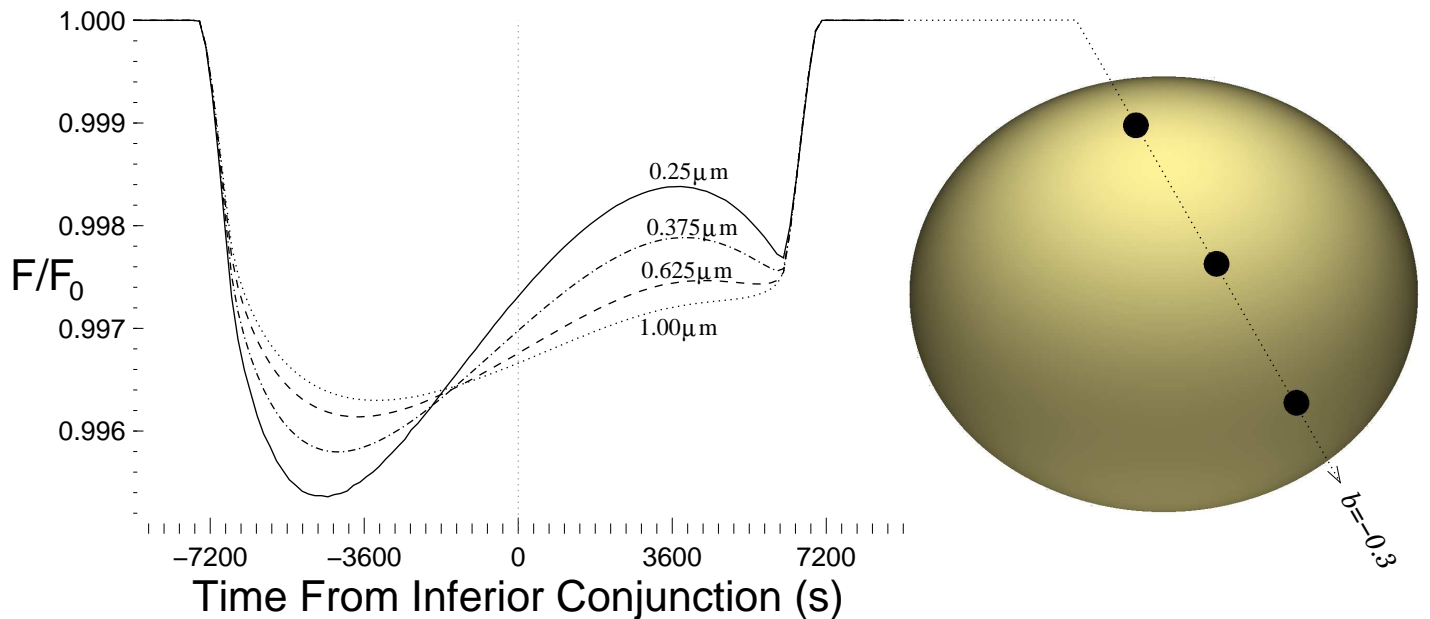


Fig. 9.— Synthetic lightcurves for transiting $1 R_{\text{Jup}}$ in a 0.05 AU orbit around an Altair-like star with $\varphi = 60^\circ$ are plotted. The 4 curves all correspond to planets with a transit impact parameter of $b = -0.3 R_{\text{pole}}$. The different curves correspond to what a lightcurve would look like if it were acquired at different wavelengths: $0.25 \mu\text{m}$ (solid line), $0.375 \mu\text{m}$ (dotted line). Note that wavelength is all that is changed here – in particular I have employed the identical limb darkening parameter of $c_1 = 0.64$ for each wavelength. Though this is unphysical in that the limb darkening should diminish with increasing wavelength, this way makes it easiest to identify just the differences due to wavelength changes. The contrast on the stellar disk is greater on the Wien (short wavelength) end of the blackbody curve, while the contrast is muted on the Rayleigh-Jeans (long wavelength) side.

show lightcurves that resemble those of planets orbiting slow-rotating stars so closely that the two cannot be distinguished based on lightcurves alone. However, fitting the lightcurves of the planets around fast-rotators with a spherical-star model yields incorrect transit parameters. The significant systematic errors introduced into the determination of the planet's radius are particularly distressing, especially at high impact parameters. This degeneracy can be resolved by independent determination of the stellar rotation period.

Planets that are not spin-orbit aligned can lead to spectacularly strange lightcurves that might not otherwise be immediately recognizable as planetary transits. Such planets can yield asymmetric lightcurves and highly curved transit floors that rule out the spherical-star hypothesis. The precise shape of such transits reveals the stellar obliquity and the angle between the transit chord and the projected stellar rotation axis. Together these two values determine the net spin-orbit alignment of the system. There is still a twofold degeneracy of the system, reflected around the projected stellar rotation axis.

The changing temperatures across the face of the stellar disk lead to strong variability of transit lightcurves as a function of wavelength. Multi-wavelength transit photometry can then directly constrain the stellar temperatures, allowing for better models of the stars themselves. High-quality stellar models lead to more reliable measurements of the planet's radius.

Perhaps $\sim 5\text{--}10\%$ of the *Kepler* target stars ought to be main sequence dwarfs of spectral type early F or earlier, and thus are probably rapid rotators. Determination of the spin-orbit alignment of planets orbiting these stars will provide a glimpse into the planet formation process around high-mass stars for the first time.

REFERENCES

- Barnes, J. W. 2007, *PASP*, 119, 986
- Barnes, J. W. & Fortney, J. J. 2003, *ApJ*, 588, 545
- . 2004, *ApJ*, 616, 1193
- Brown, T. M., Charbonneau, D., Gilliland, R. L., Noyes, R. W., & Burrows, A. 2001, *ApJ*, 552, 699
- Ciardi, D. R., van Belle, G. T., Akeson, R. L., Thompson, R. R., Lada, E. A., & Howell, S. B. 2001, *ApJ*, 559, 1147
- Djurašević, G., Rovithis-Livaniou, H., Rovithis, P., Georgiades, N., Erkapić, S., & Pavlović, R. 2003, *A&A*, 402, 667
- Hansen, C. J., Kawaler, S. D., & Trimble, V. 2004, *Stellar interiors : physical principles, structure, and evolution* (Stellar interiors : physical principles, structure, and evolution, 2nd ed., by C.J. Hansen, S.D. Kawaler, and V. Trimble. New York: Springer-Verlag, 2004.)
- Hébrard, G., Bouchy, F., Pont, F., Loeillet, B., Rabus, M., Bonfils, X., Moutou, C., Boisse, I., Delfosse, X., Desort, M., Eggenberger, A., Ehrenreich, D., Forveille, T., Lagrange, A.-M., Lovis, C., Mayor, M., Pepe, F., Perrier, C., Santos, N. C., Queloz, D., Ségransan, D., Udry, S., & Vidal-Madjar, A. 2009, in *IAU Symposium*, Vol. 253, *IAU Symposium*, 508–511
- Johnson, J. A., Fischer, D. A., Marcy, G. W., Wright, J. T., Driscoll, P., Butler, R. P., Hekker, S., Reffert, S., & Vogt, S. S. 2007, *ApJ*, 665, 785
- Johnson, J. A., Marcy, G. W., Fischer, D. A., Wright, J. T., Reffert, S., Kregenow, J. M., Williams, P. K. G., & Peek, K. M. G. 2008a, *ApJ*, 675, 784
- Johnson, J. A., Winn, J. N., Narita, N., Enya, K., Williams, P. K. G., Marcy, G. W., Sato, B., Ohta, Y., Taruya, A., Suto, Y., Turner, E. L., Bakos, G., Butler, R. P., Vogt, S. S., Aoki, W., Tamura, M., Yamada, T., Yoshii, Y., & Hidas, M. 2008b, *ApJ*, 686, 649
- Jurić, M. & Tremaine, S. 2008, *ApJ*, 686, 603
- Kalas, P., Graham, J. R., Chiang, E., Fitzgerald, M. P., Clampin, M., Kite, E. S., Stapelfeldt, K., Marois, C., & Krist, J. 2008, *Science*, 322, 1345
- Liu, Y.-J., Sato, B., Zhao, G., & Ando, H. 2009, *Research in Astronomy and Astrophysics*, 9, 1
- Lovis, C. & Mayor, M. 2007, *A&A*, 472, 657
- Maeder, A. 2009, *Physics, Formation and Evolution of Rotating Stars* (Physics, Formation and Evolution of Rotating Stars: , Astronomy and Astrophysics Library, Volume . ISBN 978-3-540-76948-4. Springer Berlin Heidelberg, 2009)
- Marois, C., Macintosh, B., Barman, T., Zuckerman, B., Song, I., Patience, J., Lafreniere, D., & Doyon, R. 2008, *Science*, 322, 1348
- Monnier, J. D., Zhao, M., Pedretti, E., Thureau, N., Ireland, M., Muirhead, P., Berger, J.-P., Millan-Gabet, R., Van Belle, G., ten Brummelaar, T., McAlister, H., Ridgway, S., Turner, N., Sturmann, L., Sturmann, J., & Berger, D. 2007, *Science*, 317, 342
- Moutou, C., Hébrard, G., Bouchy, F., Eggenberger, A., Boisse, I., Bonfils, X., Gravallon, D., Ehrenreich, D., Forveille, T., Delfosse, X., Desort, M., Lagrange, A.-M., Lovis, C., Mayor, M., Pepe, F., Perrier, C., Pont, F., Queloz, D., Santos, N. C., Ségransan, D., Udry, S., & Vidal-Madjar, A. 2009, *A&A*, 498, L5
- Narita, N., Hirano, T., Sato, B., Winn, J. N., Suto, Y., Turner, E. L., Aoki, W., Tamura, M., & Yamada, T. 2009, *ArXiv e-prints*
- Niedzielski, A., Goździewski, K., Wolszczan, A., Konacki, M., Nowak, G., & Zieliński, P. 2008, *ArXiv e-prints*
- Niedzielski, A., Konacki, M., Wolszczan, A., Nowak, G., Maciejewski, G., Gelino, C. R., Shao, M., Shetrone, M., & Ramsey, L. W. 2007, *ApJ*, 669, 1354

- Peterson, D. M., Hummel, C. A., Pauls, T. A., Armstrong, J. T., Benson, J. A., Gilbreath, G. C., Hindsley, R. B., Hutter, D. J., Johnston, K. J., Mozurkewich, D., & Schmitt, H. 2006a, *ApJ*, 636, 1087
- Peterson, D. M., Hummel, C. A., Pauls, T. A., Armstrong, J. T., Benson, J. A., Gilbreath, G. C., Hindsley, R. B., Hutter, D. J., Johnston, K. J., Mozurkewich, D., & Schmitt, H. R. 2006b, *Nature*, 440, 896
- Pont, F., Hébrard, G., Irwin, J. M., Bouchy, F., Moutou, C., Ehrenreich, D., Guillot, T., & Aigrain, S. 2009, *ArXiv e-prints*
- Press, W. H., Teukolsky, S. A., Vetterling, W. T., & Flannery, B. P. 1992, *Numerical recipes in C. The art of scientific computing* (Cambridge: University Press)
- Robinson, S. E., Laughlin, G., Vogt, S. S., Fischer, D. A., Butler, R. P., Marcy, G. W., Henry, G. W., Driscoll, P., Takeda, G., & Johnson, J. A. 2007, *ApJ*, 670, 1391
- Russell, H. N. 1939, *ApJ*, 90, 641
- Sato, B., Izumiura, H., Toyota, E., Kambe, E., Ikoma, M., Omiya, M., Masuda, S., Takeda, Y., Murata, D., Itoh, Y., Ando, H., Yoshida, M., Kokubo, E., & Ida, S. 2008a, *PASJ*, 60, 539
- Sato, B., Toyota, E., Omiya, M., Izumiura, H., Kambe, E., Masuda, S., Takeda, Y., Itoh, Y., Ando, H., Yoshida, M., Kokubo, E., & Ida, S. 2008b, *PASJ*, 60, 1317
- Seager, S. & Hui, L. 2002, *ApJ*, 574, 1004
- Snellen, I. A. G., Koppenhoefer, J., van der Burg, R. F. J., Dreizler, S., Greiner, J., de Hoon, M. D. J., Husser, T. O., Kruhler, T., Saglia, R. P., & Vuijsje, F. N. 2008, *ArXiv e-prints*
- Triaud, A. H. M. J., Queloz, D., Bouchy, F., Moutou, C., Collier Cameron, A., Claret, A., Barge, P., Benz, W., Deleuil, M., Guillot, T., Hébrard, G., Lecavelier des Étangs, A., Lovis, C., Mayor, M., Pepe, F., & Udry, S. 2009, *ArXiv e-prints*
- von Zeipel, H. 1924, *MNRAS*, 84, 665
- Winn, J. N., Johnson, J. A., Marcy, G. W., Butler, R. P., Vogt, S. S., Henry, G. W., Roussanova, A., Holman, M. J., Enya, K., Narita, N., Suto, Y., & Turner, E. L. 2006, *ApJ*, 653, L69
- Winn, J. N., Johnson, J. A., Peek, K. M. G., Marcy, G. W., Bakos, G. Á., Enya, K., Narita, N., Suto, Y., Turner, E. L., & Vogt, S. S. 2007, *ApJ*, 665, L167
- Wolf, A. S., Laughlin, G., Henry, G. W., Fischer, D. A., Marcy, G., Butler, P., & Vogt, S. 2007, *ApJ*, 667, 549